# Nozzleless Acoustic Droplet Ejector with Electrically Tunable Droplet Size for Picking and Placing Semiconductor Chips

Yongkui Tang, *Graduate Student Member, IEEE*, and Eun Sok Kim, *Fellow*, *IEEE*

***Abstract*—This paper presents a microfabricated nozzleless acoustic droplet ejector with electrically tunable droplet size as a new tool for *on-demand* picking and placing semiconductor chips for semiconductor packaging. The ejector is based on a 2-mm-thick lead zirconate titanate (PZT) sheet with a planar annular-ring air-cavity acoustic Fresnel lens on top. When driven with sinusoidal pulsed voltage signals of 1.16 MHz, the ejector generates focused ultrasound with 1-mm focal diameter and 5-mm focal depth at 22 mm focal length in sodium polytungstate (SPT) solution. A finite-element-method (FEM) simulation model calculating the acoustic-field-induced fluid motion during the droplet ejection process has been developed, and verified by experiments, in which the device ejects SPT droplets whose diameter is from 850 to 2,490 µm, controlled by the driving pulse width and voltage. The ejected droplets are able to carry 400-µm-thick square silicon chips with side length from 700 to 3,100 µm. A polyester channel-embedded guiding cover for semi-automatic loading of silicon chips to the ejection site is designed to avoid manual placement of the silicon chips. With the proof-of-concept system, we demonstrate ejecting silicon chips out of SPT surface onto a nearby paper, assembling them into arrays with 5 mm interval between chips.**

***Index Terms*—Acoustic droplet ejection, focused ultrasound, finite-element-method simulation, fluid dynamics, acoustic lens, semiconductor packaging, ultrasonic transducer.**

## I. Introduction

In semiconductor packaging such as the assembly of surface mount devices (SMD) or micro-light-emitting diodes (micro-LED), individual chips need to be precisely picked and placed onto various substrates, and a sophisticated system equipped with robotic arms each carrying multiple nozzles with vacuum suction is commonly used for such tasks [1]. The system is usually expensive and bulky due to its complexity. With many moving parts, mechanical failures become a concern, and building a system with massively parallel processing capability is highly challenging. The nozzles in the system, handling tens of thousands parts per hour, suffer from wear and tear that can cause deformation and damage, which may lead to loss of vacuum (and thus holding power), shifts in picking or placing positions, or even part damage, increasing the assembly failure rate [2]. In addition, the nozzle size limits the system's ability to handle very small chips, and different nozzle size is needed in order to handle chips of different sizes. As a result, a cheaper and smaller system having no moving parts or nozzles, and with the capability for massively parallel processing and handling very small chips is highly desirable. To realize such a system, we come up with the idea of utilizing liquid droplets ejected by high-intensity acoustic waves to carry semiconductor chips to the target position.

Acoustic droplet ejection (ADE) was first reported in scientific literature in 1927 [3], where oil droplets were observed to be ejected from the liquid surface by continuous acoustic waves of high energy generated by a piezoelectric quartz resonator. In 1989, this phenomenon was systemically studied with both experiments and numerical simulations using tone bursts of focused acoustic energy [4]. The high energy from focused acoustic waves can overcome restraining forces from surface tension and gravity to eject liquid droplets at high speed without relying on physical contact or nozzles, which reduces maintenance cost and the risk of contact contamination. The technology also works with a wide range of liquids such as water [4], isopropyl alcohol (IPA) and ethanol [5], acetone and photoresist [6], ink [7], liquid metal [8], and various reagents used in life sciences [9–12], and the ejection direction as well as droplet volume can be controlled with high accuracy and precision [13]. These attractive features lead to the development of simple and cost-efficient ADE tools that use ejected droplets to transfer liquids or solids for applications such as inkjet printing [7], bio-reagent transferring [9–10], cell transferring [11–12], microsphere delivery [14], DNA [15] and protein [16] synthesis, and crystallography [17].

To effectively generate high-intensity ultrasound for droplet ejection, the acoustic waves generated by a transducer has to be focused, and curved surfaces on the transducer itself [18] or acoustic lens attached to it [4] have been used for focusing. However, curvature error and surface roughness of these usually macro-machined or 3D-printed curved surfaces are hard to control. Alternatively, focusing can be realized by controlling the time delay of the driving signal applied on each element of a phased array [19], which involves complicated driving electronics with many electrical connections, making the system bulky and complex. Another method to focus ultrasound is to use a thin, planar, microfabricated Fresnel acoustic lens. Single- [20] and multi-layer [5] acoustic Fresnel lenses have been microfabricated through etching and bonding

This work was supported by National Science Foundation under grant number CNS 1716953. The authors are with the Department of Electrical and Computer Engineering, University of Southern California, Los Angeles, CA 90089-0271, USA (emails: yongkuit@usc.edu and eskim@usc.edu).

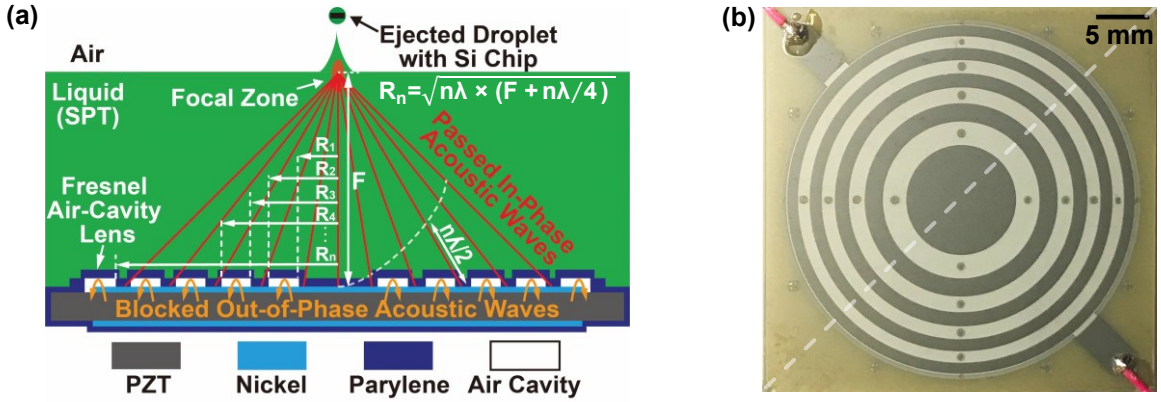


Fig.1. (a) Schematic showing the cross section (across the dashed line in (b)) of the droplet/silicon chip ejector, to illustrate how the annular-ring air-cavity Fresnel lens is designed to focused ultrasound. (b) Top-view photo of the ejector on 2-mm-thick PZT substrate (brown), showing five air-cavity rings (light grey with holes, for blocking out-of-phase waves) alternating with five Parylene-covered electrode regions (dark grey circle and rings, where in-phase waves could pass). The four holes on each air-cavity ring are release-holes sealed after releasing sacrificial layers to create the air cavities during fabrication [21].

to thin-film transducers, with challenges in precisely controlling the layer thickness. On the other hand, our fully-microfabricated self-focusing acoustic transducers (SFATs) [21] with annular-ring air-cavity Fresnel lenses are easy to be manufactured since the layer thickness control is not critical, and no bonding of the lens is needed. With our SFAT-based droplet ejectors, the demonstrated ejection rate is up to 8 kHz [22], and the transducers can be formed into arrays for parallel ejection of multiple droplets [15−16]. Moreover, the size of droplets ejected by the SFATs can be tuned through electrically controlling the number of activated Fresnel rings [23] or designing transducers working at different frequencies [14, 22]. These advantages make SFAT-based droplet ejectors a good tool for semiconductor chip ejection. However, the previous SFAT-based droplet ejectors have relatively small droplet size (up to 560 μm [23]), which is not large enough to generate droplets for carrying most semiconductor chips.

In this work, as a proof-of-concept demonstration, we present a simple system based on our newly designed SFAT-based droplet ejector, which achieves a focal size as large as 1 mm, and can eject droplets to carry silicon chips floating on liquid surface. The transducer has small footprint and can be electrically interfaced with only two electrical wires. We also demonstrate a new and easy way to control the droplet size through changing the driving pulse width and voltage, which can vary the droplet diameter for transferring chips of various sizes. Moreover, we design a channel-embedded plastic cover to load silicon chips automatically onto the ejection site by the local fluid flow generated during droplet ejection.

## II. Device Design

The SFAT is built on a bulk PZT substrate on top of which a nickel electrode is patterned into a circle with an extended rectangular soldering pad for electrical connection (Fig. 1b). At the bottom side of the PZT, another electrode is patterned into the same shape but with a 90° rotation so that the circular portions of both electrodes coincide but the soldering pads do not. When sinusoidal voltage signal is applied across the electrodes through electrical wires soldered on the rectangular pads, the PZT sandwiched between the circular regions of the electrodes vibrates in thickness direction, generating acoustic waves, which are focused through a planar acoustic Fresnel lens on the top electrode. The lens consists of Parylene-sealed annular-ring air cavities alternating with non-air-cavity circle and ring areas that are uniformly coated with Parylene (Fig. 1a and 1b). The acoustic waves are almost completely blocked by the air cavities due to the large acoustic impedance difference between air (0.4 kPa·s/m) and solid (over 1 MPa·s/m), but can propagate through the non-air-cavity areas. To focus ultrasound waves at a focal point at a distance $F$ (focal length) above the center of the transducer's top surface, the annular rings are designed into Fresnel half-wavelength bands (FHWB) [20] so that all the acoustic waves arrive at the focal point with a net phase difference less than 180° after passing through the lens. This is achieved by choosing boundary radii $R_n$ so that the path-length from the focal point to any ring boundary is longer than $F$ by integer multiples of the half wavelength ($\lambda/2$) (Fig. 1a), as shown in the equation below:

$$\sqrt{R_n^2+F^2}-F=n\lambda/2\,,n=0,1,2,\cdots, \quad (1)$$

from which we have:

$$R_n=\sqrt{n\lambda\times(F+n\lambda/4)},n=0,1,2,\cdots. \quad (2)$$

The non-air-cavity regions are assigned for areas where $R_n < R < R_{n+1}, n=0,2,4,\cdots$, which include the circle in the center (which is essentially a "ring" with zero inner diameter) and every other ring outward.

Since the droplet size is proportional to the focal diameter [4−5, 14, 22−23], to have large droplet size, we design the Fresnel lens to have a large focal diameter, which can be approximated by the width of the outermost ring band (if its boundary radii are much larger than its width) of the lens [14]. For a Frensel lens with total $N$ ring boundaries with the outermost ring width being $\Delta R$, if $R_N \gg \Delta R$ (which is usually true for $N \geq 5$), we have [14]:

$$\Delta R \cong \sqrt{(cF)/(4Nf)}, \quad (3)$$

where $f$ and $c$ are frequency and sound velocity in medium, respectively. According to (3), in order to make focal diameter large (which can be estimated by $\Delta R$), we design a SFAT with long focal length of 22 mm, low operating frequency of 1.16 MHz, and only five non-air-cavity Fresnel rings ($N = 9$).

TABLE I
KEY SIMULATION SETTINGS*

| | Acoustic Simulation | | Fluid Dynamics Simulation |
|---|---|---|---|
| **Simulation Area** | Area ABPO | | Area CDNM |
| **Material** | Ignoring SPT-air interface reflection: SPT: Area ABPO | Normal cases: Air: Area ABJG SPT: Area GJPO | At t =0, Air: Area CDIG SPT: Area GINM |
| **Physics Modules** | Pressure Acoustics, Frequency domain | | Laminar Flow/Level Set, Time domain |
| **Boundary Conditions** | Normal displacement (non-air-cavity rings): $OR_1$, $R_2R_3$, $R_4R_5$, $R_6R_7$, $R_8R_9$; Sound hard boundaries (air-cavity rings): $R_1R_2$, $R_3R_4$, $R_5R_6$, $R_7R_8$, $R_9P$; Perfectly matched boundaries (no reflection): ABJP | | Volume force: Area EFLK, value derived from acoustic simulation, duration equal to pulse width; Gravity: Area CDNM; Open boundary: CDNM; Level set initial interface: GHI |
| **Mesh Type/Size** | Free triangular, 25 μm maximum element size, with three rounds of adaptive mesh refinement | | Free triangular, 50 μm maximum element size, with three rounds of adaptive mesh refinement |

*All boundary and area notations are defined in Fig. 2a.

To keep silicon chips (having a density of 2.32 g/cm$^3$) afloat on liquid medium, we choose sodium polytungstate (SPT, Geoliquids Inc.) solution as liquid medium, with its density adjusted to 2.50 g/cm$^3$ by mixing SPT powder with DI water at a weight ratio of 3.386:1, resulting a sound velocity of 1,372 m/s [24]. Compared to other types of heavy liquids such as halogenated hydrocarbons, SPT solution is non-toxic, easy to make (water-soluble), and chemically inert to common materials used on semiconductor chips.

## III. SIMULATION

### A. Overview of Simulation Settings

Acoustic fields and induced fluid motions during droplet ejection have been simulated through finite-element-method (FEM) with COMSOL Multiphysics, using the settings summarized in Table I. To save computation time and memory, two-dimensional (2D) axisymmetry is defined in all simulations, where only a half of the volume cross section is modelled, as shown in Fig. 2a. All 2D simulation plots presented in this paper are created through mirroring the simulated data along the central vertical axis ($R$ = 0). In the simulations, only the media (SPT and/or air) above the transducer are considered, and the acoustic waves coming from the transducer are modelled with normal displacement boundary conditions on the non-air-cavity areas.

In acoustic simulations, the reflection from sidewalls are ignored by adding perfectly matched boundary layers, since the sidewalls are reasonably far away from the focal point of the transducer in the actual cases. The simulation area for fluid dynamics simulations is chosen to be smaller than that for acoustic simulations, since only the fluid motion near the central axis and the air-SPT interface are of importance.

### B. Simulation of Acoustic Pressure and Body Force

Without reflection from SPT solution's top surface, acoustic simulations in the frequency domain at 1.16 MHz show that the focal length is at the targeted 22 mm, while focal depth and diameter are 5 mm (Fig. 2b) and 1 mm (Fig. 2c), respectively. The large focal depth is desirable, because it tolerates the liquid level change during ejection. These results are confirmed with hydrophone measurement of acoustic pressure. With a SFAT immersed in SPT solution driven with 1.16 MHz sinusoidal pulsed signals, a hydrophone (HGL-0085, Onda Corp.) is scanned along the central vertical axis (Fig. 2d) and along the central lateral axis at the focal plane (Fig. 2e) to measure pressure distribution, with liquid's top surface well above the scan path to minimize reflection. The measured focal length, focal depth and focal size are 21.7, 5.03, and 1.0 mm, respectively, close to the simulated values. With 85 $V_{pp}$ applied, the peak pressure at the focal point is measured to be 1.29 MPa. In the actual case, acoustic reflection from the SPT's top surface needs to be considered. By comparing models with different liquid heights in simulation, we find that when the liquid level is 20.04 mm above the transducer, focal zones with very high pressure appear near the SPT-air interface. Through normalizing the simulated pressure value with hydrophone measurement data (assuming the peak pressure is proportional to the applied voltage), the peak pressure near the SPT's top surface is 8.7 MPa, when 400 $V_{pp}$ is applied on the transducer (Fig. 2f).

From Nyborg's analysis of Navier-Stokes equation of fluid mechanics and the continuity equation using the method of successive approximations [25], the acoustic-field-induced steady body force $\overrightarrow{F_{ac}}$ exerted on the SPT solution (which is considered as an incompressible Newtonian fluid) can be evaluated using the equation below:

$$\overrightarrow{F_{ac}} = \rho_{SPT}\langle\overrightarrow{v_1}\,(\nabla\cdot\overrightarrow{v_1}) + (\overrightarrow{v_1}\cdot\nabla)\overrightarrow{v_1}\rangle, \quad (4)$$

where the angle brackets denote time-averaging; $\rho_{SPT}$ is SPT density (2.50 kg/m$^3$); and $\overrightarrow{v_1}$ is sinusoidal particle velocity induced by acoustic field, calculated from simulated acoustic pressure [26]. From (4), the magnitude and direction of the body force near the SPT-air interface are evaluated (Fig. 2g), in which we clearly see strong force pointing from the center of the focal zone closest to SPT's top surface into the air, and the peak force magnitude is as high as $3.38\times10^7$ N/m$^3$.

### C. Simulation of the Droplet Ejection Process

We then use the calculated body force to simulate the droplet ejection process in time domain. For simplicity, we only model the body force near the focal zone (Area EFLK in Fig. 2a), due

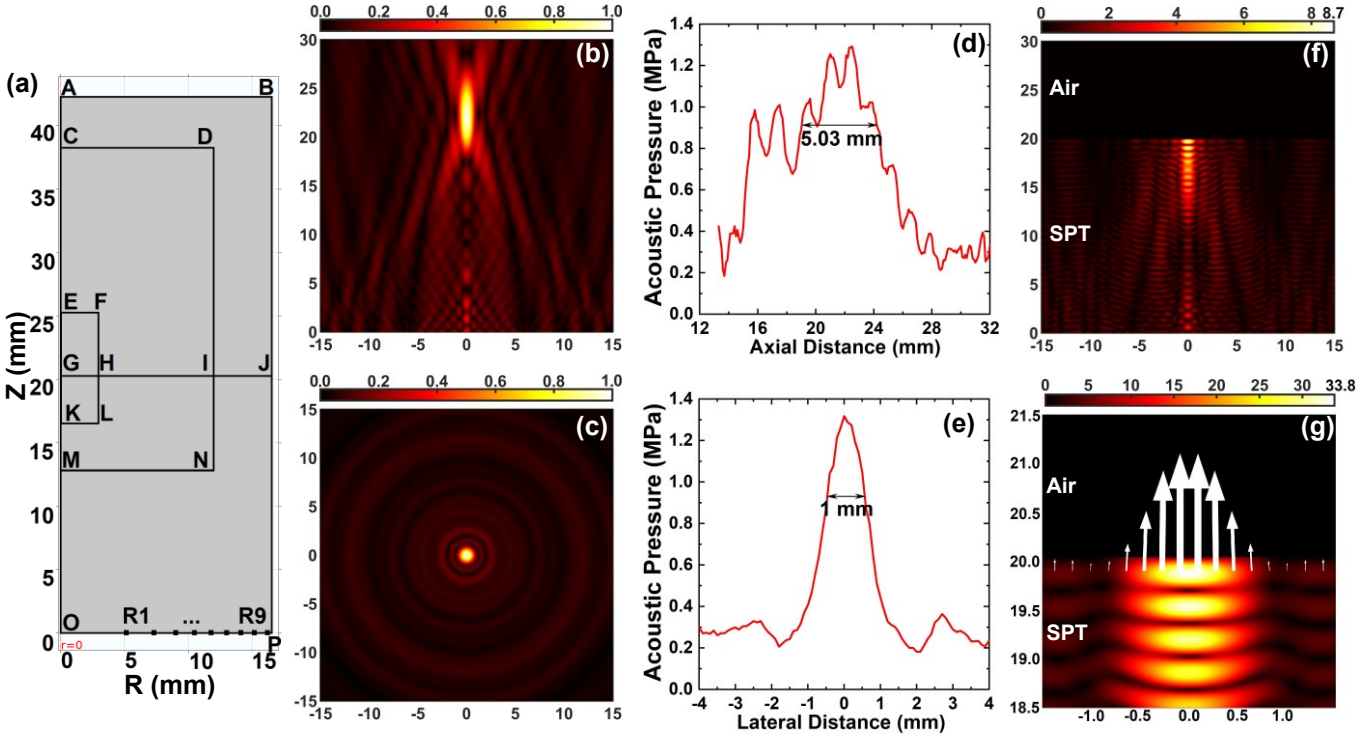


Fig. 2. (a) Defined 2D simulation area with axisymmetry, with related simulation settings shown in Table I. Simulated relative acoustic pressure distribution ignoring reflection from the SPT-air interface: (b) over the central vertical plane, (c) over focal plane at $Z$ = 22 mm. Hydrophone measurement of acoustic pressure in SPT solution (d) along the central vertical axis and (e) along the central lateral axis on the focal plane, with 85 $V_{pp}$ applied on the ejector. (f) Simulated acoustic pressure (color-bar unit: MPa) over central vertical plane with acoustic reflection from the SPT-air interface (20.04 mm above the device's top surface), with 400 $V_{pp}$ applied to the transducer (pressure values normalized from measurement data in (d) and (e)). (g) Magnitude (color-bar unit: $\times 10^6$ N/m$^3$) and direction (white arrows) of the acoustic-field-induced body force near the SPT-air interface, calculated from the pressure distribution in (f).

to the dominantly higher force magnitude in this region. To model the pulsed driving signal, the force value is multiplied by a window function whose duration is equal to the driving pulse width. In the simulation, fluid velocity $\vec{u}$ is calculated through solving the Navier-Stokes equation (5) and the continuity equation (6):

$$\rho\partial\vec{u}/\partial t + \rho\vec{u}(\nabla\cdot\vec{u}) - \eta\nabla^2\vec{u} + \nabla p = \overrightarrow{F_{ac}} + \overrightarrow{F_{st}} + \rho g, \quad (5)$$

$$\nabla\cdot\vec{u} = 0, \quad (6)$$

where $\rho$ is mass density ($1.204\times10^{-3}$ g/cm$^3$ for air [27] and 2.5 g/cm$^3$ for SPT); $\eta$ is dynamic viscosity ($1.825\times10^{-2}$ mPa·s for air [27] and 10.2 mPa·s for SPT [28]); $p$ is pressure; $g$ is standard gravity (9.8 m/s$^2$); and $\overrightarrow{F_{st}}$ is the body force induced by surface tension.

The boundary profile change of the SPT-air two-phase system is numerically solved with a conservative level set method [29]. A field function $\phi(\vec{x},t)$ having a value between 0 and 1 at any spatial coordinate $\vec{x}$ is used to model the two-phase fluid system consisting of air and SPT. The regions where $\phi = 0$ are considered as air, and the regions where $\phi = 1$ are considered as SPT, while the transition regions with $\phi$ values in between are modelled with a smoothed Heaviside step function [29], with $\phi = 0.5$ defined as the boundary between the two media. The governing equation calculating the time-evolution of the field function is shown below:

$$\partial\phi(\vec{x},t)/\partial t + \vec{u}\cdot\nabla\phi = \gamma\nabla\cdot[\epsilon_{ls}\nabla\phi - \phi(1-\phi)(\nabla\phi/|\nabla\phi|)], \quad (7)$$

where reinitialization parameter $\gamma$ and interface thickness-controlling parameter $\epsilon_{ls}$ are two non-physical parameters related to the stability and accuracy of the numerical calculation, with the former set as the maximum fluid velocity during the ejection process, while the latter being the half of the maximum finite-element mesh size. The body force from surface tension $\overrightarrow{F_{st}}$ is calculated from the interface unit normal vector $\hat{n}$ and the mean boundary curvature $\kappa$ at the SPT-air boundary, which are functions of $\phi$, as shown below [30]:

$$\hat{n} = (\nabla\phi/|\nabla\phi|)\,|_{\phi=0.5}, \quad (8)$$

$$\kappa = (-\nabla\cdot\hat{n})\,|_{\phi=0.5}, \quad (9)$$

$$\overrightarrow{F_{st}} = \sigma\kappa\delta_s\hat{n}, \quad (10)$$

where $\sigma$ is the surface tension at the SPT-air interface (78 mN/m [28]), and $\delta_s$ is a smoothed Dirac delta function centered at the boundary where $\phi = 0.5$ [30]. In each time step of the simulation, the flow velocity $\vec{u}$ is solved using (5) and (6), and then plugged into (7) to solve the field function $\phi$. Once the field function is updated, the surface-tension-induced body force $\overrightarrow{F_{st}}$ is calculated using (10), and is fed back to (5) for further updating $\vec{u}$. This process repeats as time proceeds.

Using the model mentioned above, we simulate different cases with the same 400 $V_{pp}$ applied on the transducer but with driving pulse from 517 to 2,586 µs (Fig. 3a to 3d). In all four cases, droplets are ejected by the focused ultrasound (with satellite droplets generat ed in the latter three cases), and the simulated diameter of the main droplets increases with the driving pulse width, ranging from 932.6 to 1690.5 µm (Fig. 4a). Similarly, we keep the driving pulse width at 1,724 µs, while varying the driving voltage from 310 to 430 $V_{pp}$, with the

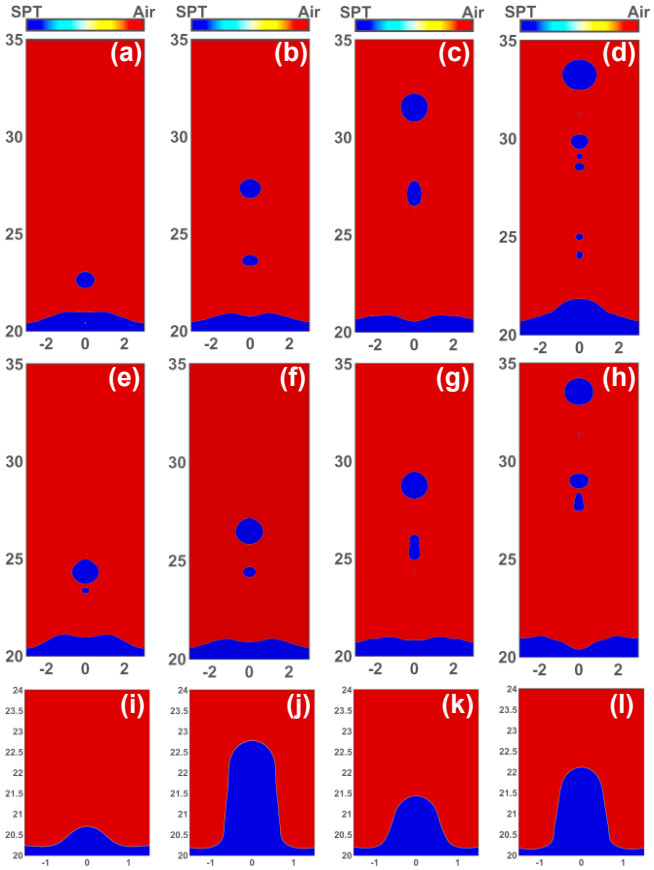


Fig. 3. Simulation snapshots of ejected droplets with 400 $V_{pp}$ applied on the transducer with driving pulse width of (a) 517 µs, (b) 862 µs, (c) 1,724 µs and (d) 2,586 µs. Simulation snapshots of ejected droplets with 1,724 µs driving pulse width and driving voltage of (e) 310 $V_{pp}$, (f) 340 $V_{pp}$, (g) 370 $V_{pp}$, and (h) 430 $V_{pp}$. Simulation snapshots of the water columns formed at the moment when acoustic signal is turned off with driving voltages and pulse widths of (i) 400 $V_{pp}$, 517 µs; (j) 400 $V_{pp}$, 2,586 µs; (k) 310 $V_{pp}$, 1,724 µs; and (l) 400 $V_{pp}$, 1,724 µs, respectively.

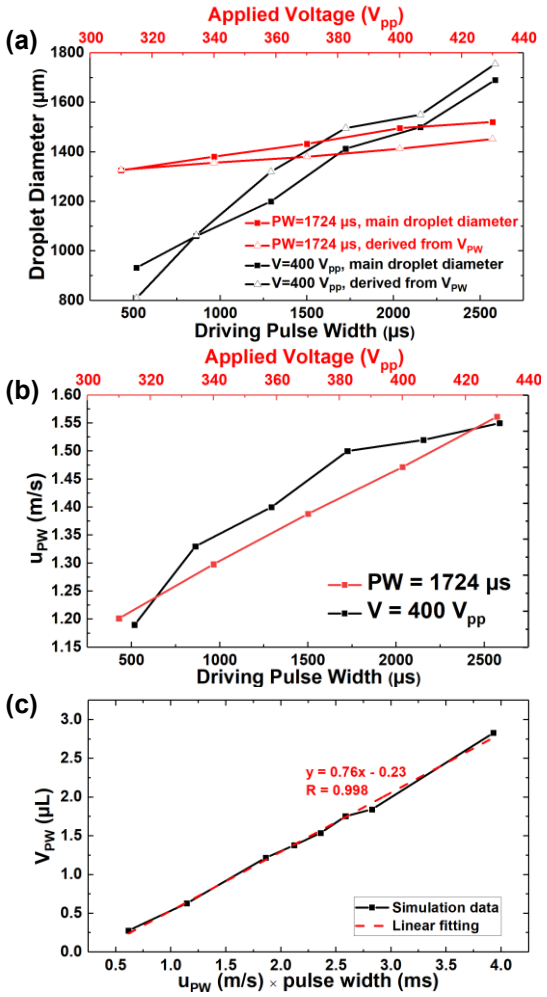


Fig. 4. (a) Simulated main droplet diameter (and the equivalent diameter calculated from the bulging water column volume $V_{PW}$ when acoustic signal is turned off) versus driving pulse width (with 400 $V_{pp}$ applied) and driving voltage (with 1,724 µs pulse width). (b) Maximum upward fluid speed along the central vertical axis ($u_{PW}$) when acoustic signal is turned off versus different driving conditions. (c) $V_{PW}$ (in µL) versus $u_{PW}$ (in m/s) multiplied by pulse width (in ms) fitted by a linear trendline.

simulated main droplet diameters shown in Fig. 4a. In this case, the droplet size also increases with applied voltage (ranging from 1327.3 to 1451.5 µm, as shown in Fig. 3c, 3e to 3h), but the increase is small compared to the case with increased pulse width.

These results suggest a new and simple way of controlling the droplet size through tuning the driving conditions, especially the pulse width. To understand this phenomenon, we have simulated the volume (defined as $V_{PW}$) of the bulging water column above the initial water surface ($Z = 20.04$ mm) at the moment when the acoustic signal (as well as the induced body force) is turned off after an activation period equal to the driving pulse width, with four examples shown in Fig. 3i–3l. To compare $V_{PW}$ and the main droplet volume in each case, we calculate the equivalent diameter from $V_{PW}$ assuming that the same amount of volume forms a spherical droplet, and plot the results in Fig. 4a. Interestingly, from the graph we see that the equivalent diameter derived from $V_{PW}$ and the main droplet diameter are very close. Although the water column will continue to rise after the acoustic signal is off, and the main droplet will break up from its tip. It seems that only the initial volume pushed up during the acoustic drive contributes to the volume of the main droplet. To study how $V_{PW}$ (which is roughly equal to the main droplet volume) is affected by the driving conditions, we also simulate the maximum upward fluid speed (defined as $u_{PW}$) along the central vertical axis ($R = 0$ mm) at the same moment when $V_{PW}$ is calculated, as shown in Fig. 4b. By plotting the product of $u_{PW}$ and the driving pulse width versus $V_{PW}$, we find a good linear relationship between these two plotted values (Fig. 4c). These findings explain the dominant effect of the pulse width on the droplet size: while both increasing applied voltage and increasing pulse width will lead to higher $u_{PW}$, an increase in the latter will further lead to higher $V_{PW}$ (and thus larger droplet size). These findings may lead to new insights on the droplet size control, and in-depth theoretical analysis regarding the physics behind them will be our future work.

## IV. With long pulse widths (and high driving voltages), the ejection process is less stable [31]. As a result, satellite droplets are generated, and the ejection direction is less repeatable. However, in our

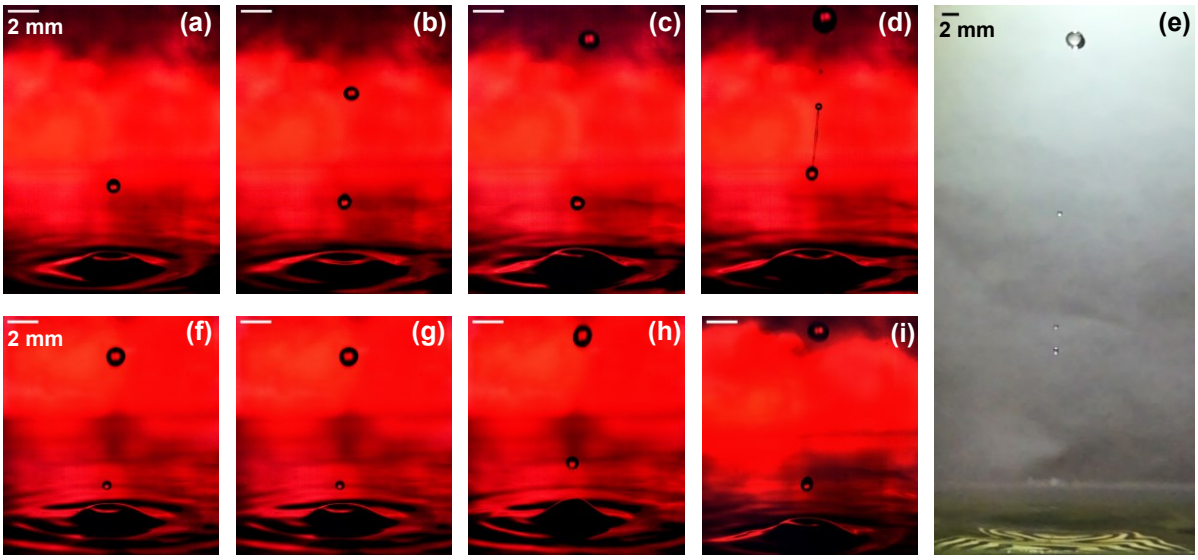


Fig. 5. Photos of the ejected droplets with 394 $V_{pp}$ applied on the transducer with driving pulse width of (a) 517 µs, (b) 862 µs, (c) 1,724 µs, (d) 2,586 µs and (e) 6,034 µs. Photos of the ejected droplets with 1,724 µs driving pulse width and driving voltage of (f) 283 $V_{pp}$, (g) 312 $V_{pp}$, (h) 339 $V_{pp}$, and (i) 368 $V_{pp}$. Scale bar length is 2 mm in all photos. All photos are taken with optical strobing, except that (e) is taken with a high-speed camera.

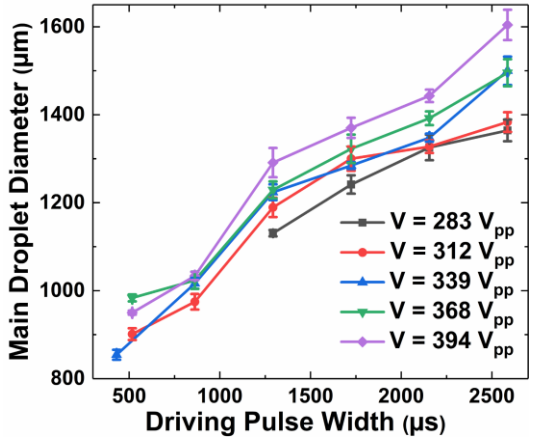


Fig. 6. Graph showing measured main droplet diameter with different driving voltages and driving pulse widths.

APPLICATION, THE FORMER CONCERN IS NOT AN ISSUE AS LONG AS THE MAIN DROPLET CAN CARRY A SEMICONDUCTOR CHIP, AND THE LATTER PROBLEM CAN BE MINIMIZED AS DISCUSSED IN THE NEXT SECTION. EXPERIMENTAL RESULTS

### *A. Characterization of Droplet Diameter*

The SFAT is microfabricated according to the steps described in [21]. During droplet ejection experiments, a 1.16 MHz pulsed sinusoidal voltage signal from a function generator (AFG3252, Tektronix, Inc.) is amplified by a power amplifier (75A250, Amplifier Research Corp.), and is delivered to the SFAT, which is placed at the bottom of a plastic container filled with SPT solution. The liquid level is adjusted until the ejected droplets can fly to the highest level before falling down due to gravity, and turn out to be around 20 mm, as predicted by the simulation in Fig. 2f. With the driving condition of 394 $V_{pp}$ and 2 Hz pulse repetition frequency (PRF) while varying the driving pulse width from 517 to 2,586 µs, we take stroboscopic snapshots of the droplet ejection process (Fig. 5a to 5d) with a long-range microscope lens (Zoom 6000, Navitar Inc.) attached to a digital camera (STC-MCCM401U3V, Sentech Co., Ltd.) which is connected to a computer to save the photos. The background during droplet ejection is illuminated by a strobing LED light source flickering at the same 2 Hz frequency with some delay after the onset of the driving voltage pulse. The droplet ejections are stable and repeatable as photos (with frame height of 15 mm) taken at different times during the ejection look almost identical, and the main droplet size increases with longer pulse width, ranging from 950 to 1,604 µm, which are close to the simulation results. With much longer pulse width of 6,034 µs, the ejection process is recorded with a high-speed camera (DSC-RX100M6, Sony Corp.) at 960 frames per second, since the ejection is less stable so that no clear image may be captured with the strobing method, and the main droplet diameter is observed to be 2,490 µm (Fig. 5e). Similarly, we vary the driving voltage from 283 to 368 $V_{pp}$, and change the pulse width in each case to measure the diameter of the ejected main droplets. In the case where the pulse width is 1,724 µs, the main droplet diameter varies from 1241.4 to 1370.2 µm, as the driving voltage changes from 268 to 394 $V_{pp}$ (Fig. 5f to 5i and 5c). All the measurement results are summarized in Fig. 6, which shows higher driving voltage and longer pulse width indeed increase the droplet size, with the pulse width having more effect on the droplet size than the voltage, especially at lower driving voltages, agreeing with simulation results in Fig. 4a.

### *B. Ejection of Silicon Chips*

We then build a setup for chip ejection based on the ejector (Fig. 7a). To simulate semiconductor chips, 400-µm-thick silicon-nitride-covered silicon wafers are diced into square pieces with a dicing saw. To guide silicon chips floating on the liquid surface to the ejection site, a 500-µm-thick polyester cover is laser-machined to create a flow channel and an engraved circle to align the cover to the center Fresnel circle of the ejector (Fig. 7b). The cover is held at the liquid surface

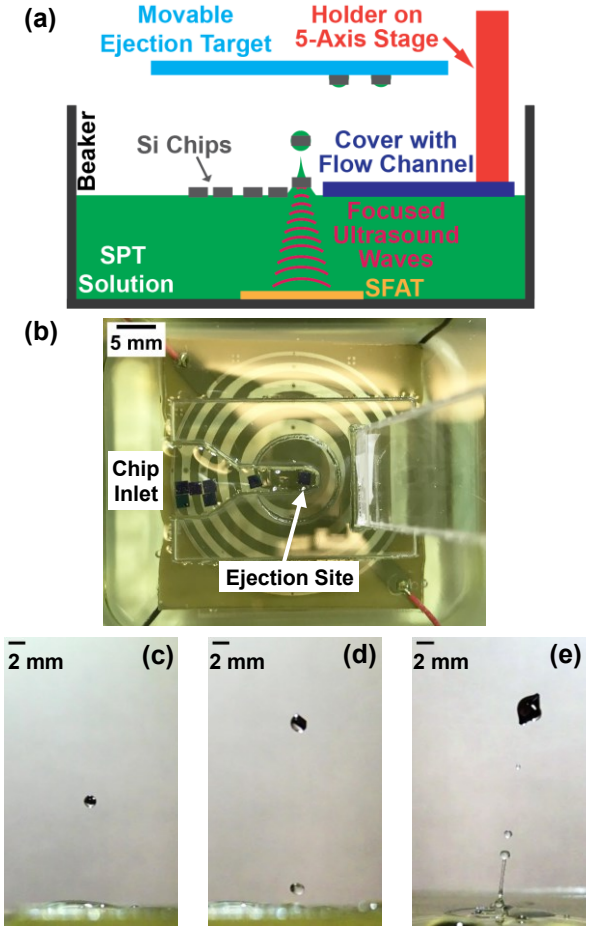


Fig. 7. (a) Cross-sectional diagram (across the center line along the channel on cover) of the ejection set-up. (b) Top-view photo of the laser-machined channel-embedded plastic cover (designed for chips with 1,600 μm side length) held by an acrylic holder, aligned to the ejector at the container bottom, with silicon chips floating in the channel. Photos of ejected droplets of differernt sizes (scale bar length: 2 mm) carrying 0.4-mm-thick silicon chips having side length of (c) 700 μm, (d) 1,600 μm (with a satellite droplet), and (e) 3,100 μm (with satellite droplets).

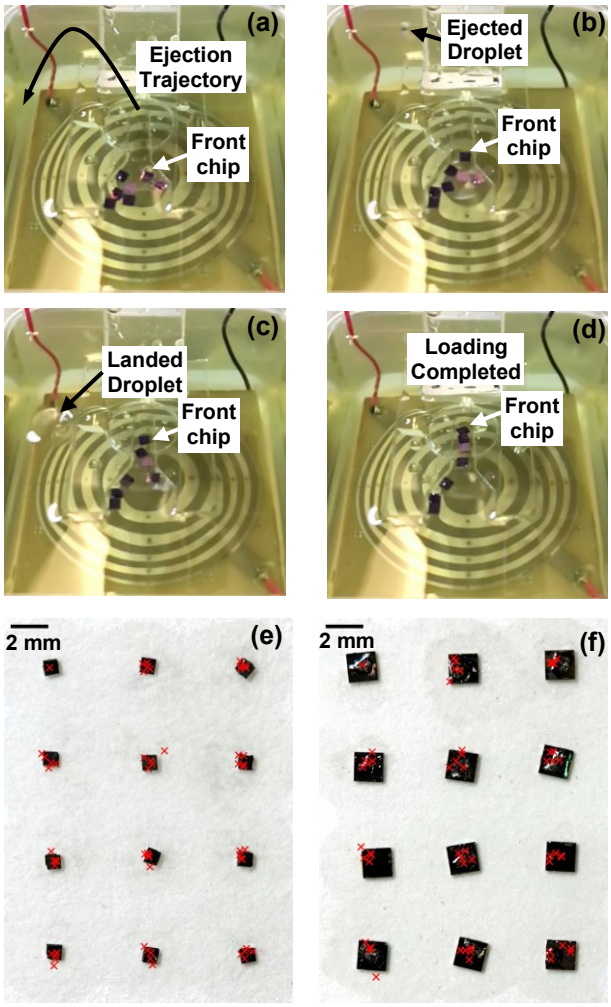


Fig. 8. Photos showing the semi-automatic chip loading mechanism: (a) chips are dumped into the inlet of the flow channel, also showing the ejection trajectory of liquid droplets under a weak ejection; (b) chips moving in along the channel as a ejected liquid droplet flies in air; (c) chips moving in further; (d) front chip loaded at the ejection site after seven ejections. Photos of 400-μm-thick square silicon chips with side length of (e) 700 μm and (f) 1,600 μm ejected into 4×3 arrays with an interval of 5 mm collected on filter paper, with red crosses showing the centers of ejected chips in five other repeated trials with the center of the left top chip aligned together.

(adjusted to around 20 mm), by a laser-machined acrylic holder fixed on a 5-axis precision stage, which allows fine-tuning of the liquid level held by surface tension between liquid and the cover as well as the alignment between the cover and the transducer. The surface tension helps also to maintain liquid height during ejection, in spite of some loss of liquid in the container from the ejection. When silicon chips are dumped onto the SPT solution (whose high density keeps them afloat) near the inlet of the cover, the chips are automatically loaded onto the ejection site, as we eject the chip one by one through operating the droplet ejector in two modes described in the next subsection. With 394 $V_{pp}$ applied to the ejector, we successfully eject droplets of different sizes to carry square silicon chips having side lengths of 700, 1600 and 3100 μm (Fig. 7c to 7e), using pulse widths of 1293, 3017, and 6034 μs, respectively.

### *C. Automatic Loading of Silicon Chips*

The chips loaded into the inlet of the embedded flow channel on the cover can be drawn to the ejection site automatically through an operating mode of weak droplet ejection. When the device is driven with 1,724 μs pulse width, 10 Hz PRF and around 200 $V_{pp}$ voltage (about half of the typical ejection voltage), due to the long pulse width and the cover not being perfectly parallel to the ejector, droplets are ejected to the side of the cover from the ejection site (Fig. 8a to 8c). The voltage is adjusted so that the droplet does not fly too high, but flies just out of the cover, so that the total liquid level remains constant. As a result, the temporarily reduced liquid level in the local area in the flow channel draws the silicon chips to the end of the channel, which is the ejection site (Fig. 8d), with the silicon chips lined up along the relatively narrow channel. When a silicon chip is in place, the loading stops automatically since the chip blocks the weak ejection. Then the driving condition is changed to the one for the regular ejection mentioned in the previous subsection (the only manual task at this point, which can be automated), and we can keep ejecting the chips lined up in the channel, until loading is needed. This process of loading and ejection can be achieved with a computer interfaced to a function generator with pre-stored conditions.

As a demonstration, a piece of filter paper is held above the liquid surface with a second movable stage which is manually moved at an interval of 5 mm after each ejection to collect the ejected chips. Once hitting the filter paper, the chip is held onto the paper by the surface tension of the SPT and is "glued" in place after water evaporates from the liquid. With a relatively large chip, the ejection is less repeatable. To ensure good positioning precision and alignment, the distance between the liquid surface and filter paper is kept short so that the chip positioning error caused by variation in ejection direction is minimized. However, if the distance is too short, sometimes the ejected chip is reflected back after hitting the paper. Thus, we find 4 mm distance to be a good compromise. In addition, since shorter driving pulse width improves ejection stability and thus repeatability, pulse widths are kept as low as possible, to 1,293 and 2,069 μs for the 700 and 1,600 μm chips, respectively. Moreover, the opening width of the guiding channel near the ejection site is designed to be close to the side length of the chip to ensure good rotational alignment (of the chips ejected and then collected). And before each ejection, we make sure that there is always a second chip right behind the loaded chip in the channel to prevent the loaded chip from going back. With these measures, we successfully eject silicon chips with side length of 700 μm (Fig. 8e) and 1,600 μm (Fig. 8f) into 4×3 arrays with the same interval. Five other trial sets indicate that the repeatability is good.

## V. Summary

This paper describes a micromachined acoustic droplet ejector based on a piezoelectric focusing ultrasonic transducer with Fresnel air-cavity lens. The transducer is capable of generating high-intensity focused ultrasound with 1-mm focal size, which can eject large liquid droplets with diameter from 850 to 2,490 μm, controlled by the driving pulse width and voltage, with the former having more tuning effect than the latter. An FEM simulation model calculating the time evolution of the acoustic-field-induced liquid motion during droplet ejection is developed, and is confirmed with experiments.

With the transducer, a proof-of-concept semiconductor chip pick-and-place system has successfully been demonstrated to eject 400-μm-thick square silicon chips with side length ranging from 700 to 3,100 μm, carried by SPT droplets of different sizes. As ejected droplets generate lateral liquid flow towards the ejection site, the chips are automatically loaded through a microchannel-embedded plastic cover.

Our experiments demonstrate that a droplet-ejector-based system that is much smaller and cheaper than the conventional approach with robotic arms can be a new possible tool for *on demand* semiconductor chip pick and placement. With easily adjustable focal size [14] and tunable droplet diameter, ejector-based pick-and-place systems are able to handle very small chips that robotic arms cannot handle reliably. In addition, since the transducer can be massively microfabricated, a similar system can potentially have massively parallel processing capability with an array of ejectors.

## References


[1] I. O. Yilmaz, "SMT placement machines," in *Development and Evaluation of Setup Strategies in Printed Circuit Board Assembly*, Wiesbaden, Germany: Gabler, 2008, ch.3, pp. 15–30.

[2] Z. Shook, "SMT preventive maintenance: Stop 5 major problems with pick-and-place nozzles." IConnect007.com. Accessed: Sep. 29, 2020. [Online]. Available: http://smt.iconnect007.com/index.php/article/52613/smt-preventive-maintenance-stop-5-major-problems-with-pick-and-place-nozzles/52616/

[3] R. W. Wood and A. L. Loomis, "The physical and biological effects of high-frequency sound-waves of great intensity," *Phil. Mag.*, vol. 4, no. 22, pp. 417–436, 1927.

[4] S. A. Elrod *et al.*, "Nozzleless droplet formation with focused acoustic beams," *J. Appl. Phys.*, vol. 65, no. 9, pp. 3441–3447, 1989.

[5] T. Hamazaki and N. Morita, "Ejection characteristics and drop modulation of acoustic inkjet printing using Fresnel lens," *J. Fluid Sci. Technol.*, vol. 4, no. 1, pp. 25–36, 2009.

[6] U. Demirci, "Acoustic picoliter droplets for emerging applications in semiconductor industry and biotechnology," *J. Microelectromech. Syst.*, vol. 15, no. 4, pp. 957–966, 2006.

[7] B. Hadimioglu, S. A. Elrod, and R. Sprague, "Acoustic ink printing: An application of ultrasonics for photographic quality printing at high speed," in *Proc. IEEE Int. Ultrason. Symp. (IUS)*, Oct. 2001, pp. 627–635.

[8] D. A. Horine, "Acoustic metal jet fabrication using an inert gas," U.S. Patent 6 007 183 A, Nov. 25, 1997.

[9] E. K. Sackmann *et al.*, "Technologies that enable accurate and precise nano- to milliliter-Scale liquid dispensing of aqueous reagents using acoustic droplet ejection," *J. Lab. Autom.*, vol. 21, no. 1, pp. 166–177, 2016.

[10] B. Colin, B. Deprez, and C. Couturier, "High-throughput DNA plasmid transfection using acoustic droplet ejection technology," *SLAS Discov. Adv. Sci. Drug Discov*., vol. 24, no. 4, pp. 492–500, 2018.

[11] U. Demirci and G. Montesano, "Cell encapsulating droplet vitrification," *Lab Chip*, vol. 7, no. 11, pp. 1428–1433, 2007.

[12] Y. Fang *et al.*, "Rapid generation of multiplexed cell cocultures using acoustic droplet ejection followed by aqueous two-phase exclusion patterning," *Tissue Eng. Part C: Methods*, vol. 18, no. 9, pp. 647–657, 2012.

[13] B. Hadimioglu, R. Stearns, and R. Ellson, "Moving liquids with sound: The physics of acoustic droplet ejection for robust laboratory automation in life sciences," *J. Lab. Autom.*, vol. 21, no. 1, pp. 4–18, 2016.

[14] Y. Tang and E. S. Kim, "Acoustic droplet-assisted particle ejection through and from agarose-gel-filled Petri dish," in *Proc. IEEE Int. Ultrason. Symp. (IUS)*, Oct. 2019, pp. 64–67.

[15] J. W. Kwon, S. Kamal-Bahl, and E. S. Kim, "In situ DNA synthesis on glass substrate for microarray fabrication using self-focusing acoustic transducer," *IEEE Trans. Autom. Sci. Eng.*, vol. 3, no. 2, pp. 152–158, 2006.

[16] Y. Choe, S.-J. Chen, and E. S. Kim, "Peptide synthesis on glass substrate using acoustic droplet ejector," *IEEE Trans. Biomed. Eng.*, vol. 61, no. 3, pp. 705–710, 2014.

[17] C. G. Roessler *et al.*, "Acoustic injectors for drop-on-demand serial femtosecond crystallography," *Structure*, vol. 24, no. 4, pp. 631–640, 2016.

[18] G. R. Lockwood, D. H. Turnbull, and F. S. Foster, "Fabrication of high frequency spherically shaped ceramic transducers," *IEEE Trans. Ultrason. Ferroelectr. Freq. Control*, vol. 41, no. 2, pp. 231–235, 1994.

[19] M. Lu *et al.*, "Design and experiment of 256-element ultrasound phased array for noninvasive focused ultrasound surgery," *Ultrasonics*, vol. 44, no. Suppl., pp. 325–330, 2006.

[20] K. Yamada and H. Shimizu, "Planar-structure focusing lens for acoustic microscope," in *Proc. IEEE Int. Ultrason. Symp. (IUS)*, Oct. 1985, pp. 755–758.

[21] Y. Tang, L. Wang, Y. Wang, and E. S. Kim, "On-demand, heatless ejection of sub-MM-sized liquid droplets," in *Proc. IEEE 30th Int. Conf. on Micro Electro Mech. Syst. (MEMS)*, Jan. 2017, pp. 1196–1199.

[22] C.-Y. Lee, H. Yu, and E. S. Kim, "Harmonic operation of acoustic transducer for droplet ejection application," in *Proc. 14th Int. Conf. Solid-State Sens. Actuators and Microsyst. (Transducers)*, Jun. 2007, pp. 1283–1286.

[23] Y. Tang and E. S. Kim, “Electrical tuning of focal size with single focused ultrasonic transducer,” in *Proc. IEEE Int. Ultrason. Symp. (IUS)*, Oct. 2018, pp. 1–4.
[24] M. Sahin, K. Ayranci, E. Kosun, and E. Ayranci, “Density, sound velocity and viscosity properties of aqueous sodium metatungstate solutions and an application of these solutions in heavy mineral separations,” *Chem. Geol.*, vol. 264, no. 1–4, pp. 96–100, 2009.
[25] W. L. Nyborg, “Acoustic streaming due to attenuated plane waves”, *J. Acoust. Soc. Am.*, vol. 25, no. 1, pp. 68–75, 1953.
[26] *COMSOL Multiphysics Version 5.5 User’s Guide on Acoustic Module*, COMSOL Inc., Burlington, MA, USA, 2019.
[27] Y. Cengel and J. Cimbala, *Fluid Mechanics: Fundamentals and Applications*, 3rd ed. New York City, NY, USA: McGraw-Hill, 2014, pp. 948.
[28] S. Natsui *et al.*, “Observation of interface deformation in sodium polytungstate solution–silicone oil system due to single rising bubble,” *ISIJ Int.*, vol. 57, no. 2, pp. 394–396, 2017.
[29] E. Olsson and G. Kreiss, “A conservative level set method for two phase flow,” *J. Comput. Phys.*, vol. 210, no. 1, pp. 225–246, 2005.
[30] *COMSOL Multiphysics Version 5.5 User’s Guide on CFD Module*, COMSOL Inc., Burlington, MA, USA, 2019.
[31] Y. Zhong, H. Fang, Q. Ma, and X. Dong, “Analysis of droplet stability after ejection from an inkjet nozzle,” *J. Fluid Mech.*, vol. 845, pp. 378–391, 2018.

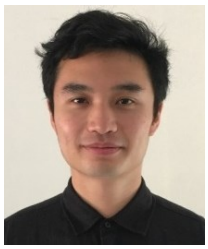

**Yongkui Tang** (Graduate Student Member, IEEE) received the B.S. degree from Peking University, Beijing, China in 2014, and the M.S. degree in electrical engineering from University of Southern California (USC), Los Angeles, CA, USA in 2016, where he is currently pursuing the Ph.D. degree in electrical engineering.

His research mainly focuses on MEMS (microelectromechanical systems), microfabrication, and piezoelectric ultrasonic transducers (especially on self-focusing acoustic transducers (SFATs) and acoustic tweezers).

**Eun Sok Kim** (Fellow, IEEE) received the B.S., M.S., and Ph.D. degrees in electrical engineering from the University of California at Berkeley, CA, USA, in 1982, 1987, and 1990, respectively.

He was with the IBM Research Laboratory, San Jose, CA, USA, NCR Corporation, San Diego, CA, USA, and Xicor Inc., Milpitas, CA, USA, as a Co-Op Student, Design Engineer, and Summer-Student Engineer, respectively. From Spring 1991 to Fall 1999, he was with the Department of Electrical Engineering, University of Hawaii at Manoa, as a Faculty Member. He joined the University of Southern California (USC) at Los Angeles, in Fall 1999, where he is currently a Professor of the Ming Hsieh Department of Electrical and Computer Engineering. From July 1, 2009 to June 30, 2018, he chaired the Electrophysics division of the department, and oversaw a net tenure-track-faculty growth of 2.5 (from 15.25 to 17.75), 6.5 new tenure-track-faculty hires, 3 new tenure-track-faculty offers and acceptances in the last year as the chair. During his tenure as the chair, US News' ranking raw score on USC EE's Graduate Program rose from 3.9 to 4.2 (out of 5.0).

He is an expert in piezoelectric and acoustic MEMS as well as electromagnetic vibration-energy harvesters (VEHs), having published about 250-refereed papers in the fields. He holds 16 issued US patents in piezoelectric and acoustic MEMS as well as in VEHs.

Dr. Kim is a Fellow of the Institute of Physics. He has received the Research Initiation Award (1991–1993) and the Faculty Early Career Development Award (1995–1999) from the National Science Foundation. He has also received the Outstanding Electrical Engineering Faculty of the Year Award from the University of Hawaii at Manoa in 1996 and the IEEE TRANSACTIONS ON AUTOMATION SCIENCE AND ENGINEERING 2006 Best New Application Paper Award. He currently serves as an Editor for the IEEE/ASME JOURNAL OF MICROELECTROMECHANICAL SYSTEMS.